DOI: 10.24874/ti.2028.09.25.12

Tribology in Industry

www.tribology.rs

RESEARCH

Optimized Supervised Machining Learning-Based Energy Efficient Optimization of Roller Burnishing Process

An-Le Van[a], Minh-Thai Le[b], Truong-An Nguyen[c], Thai-Chung Nguyen[c], Huu-Toan Bui[c], Huu-Phan Nguyen[d], Trung-Thanh Nguyen[c,*]

[a]*Faculty of Engineering and Technology, Nguyen Tat Thanh University, Ho Chi Minh City, Vietnam,*
[b]*Faculty of Special Equipments, Le Quy Don Technical University, Hanoi, Vietnam,*
[c]*Faculty of Mechanical Engineering, Le Quy Don Technical University, Hanoi, Vietnam,*
[d]*School of Mechanical and Automotive Engineering, Hanoi University of Industry, Hanoi, Vietnam.*

Keywords:

Roller burnishing
Energy consumed
Roughness
Hardness
Optimized XGBoost
Grasshopper Optimization Algorithm

* Corresponding author:

Trung-Thanh Nguyen
E-mail:
trungthanhnguyen@lqdtu.edu.vn

Received: 22 September 2025
Revised: 28 October 2025
Accepted: 15 December 2025

A B S T R A C T

In this work, the burnishing parameters, including the spindle speed (S), feed rate (f), depth of penetration (D), and number of rollers (N) are optimized to maximize the Vickers hardness (VH) and minimize energy consumption (EC) as well as average surface roughness (Ra). Predictive models of burnishing responses are proposed using the optimized Extreme Gradient Boosting (OXGBoost) approach. An efficient algorithm entitled Grasshopper Optimization Algorithm (GOA) is used to create optimal solutions. The entropy method and Pareto-Edgeworth Grierson (PEG) are utilized to calculate weights and select the best data. The findings presented that the optimal S, f, D, and N are 1075 rpm, 0.07 mm/z, 0.06 mm, and, respectively. At the optimal point, the VH is enhanced by 5.1%, while the EC and Ra are reduced by 5.4% and 23.3%, respectively. The EC model was significantly affected by the f, S, N, and D, respectively. The Ra model was significantly affected by the D, f, N, and S, respectively. The VH model was significantly affected by the D, N, f, and S, respectively. The OXGBoost-Entropy-GOA-PEG was a prominent solution to deal with complicated optimization issues, as compared to the conventional one. The outcomes can be applied to enhance energy efficiency and surface properties of the burnishing AISI 5140 process.

1. INTRODUCTION

Roller burnishing is an effective finishing technique that produces high-quality surface finishes for machined products. Better surface properties of the burnished workpiece include reduced friction, enhanced wear resistance, higher compressive residual stress, and decreased roughness. As a result, various surfaces and materials are effectively machined using the burnishing technique.

Different burnishing operations have been optimized using various optimization approaches to improve the performance outcomes. The optimal *S*, *f*, burnishing force, and the number of passes of the roller burnishing Mg-SiC metal matrix process were selected to improve the surface properties and geometrical accuracy. The results presented that the optimal *Ra*, *VH*, and circularity were 0.15 μm, 57.9 HV, and 0.015 mm, respectively [1]. Beşliu-Băncescu and Slătineanu indicated that the *Ra* and machining force of the MQL-based burnishing EN AW-2007 process were decreased by 18.0% and 4.0%, respectively, as compared to the dry condition [2]. The RSM models of the *Ra*, *VH*, and residual stress of the burnished AA6061-T6 were proposed in terms of process parameters [3]. The results revealed that the burnishing responses were primarily affected by the *f* and *S*, respectively. An ultrasonic burnishing process was developed to improve the surface properties of the burnished 20Cr2Ni4A steel [4]. The results indicated that the *Ra* and *MH* were improved by 84.5% and 58.2%, respectively. The RSM model of the *Ra* was developed for the burnished S235JR steel [5]. The results showed that the responses are primarily affected by the burnishing force and ball diameter, respectively. The non-rotary flat slide ball burnishing was developed to enhance surface properties of the milled AA7075-T651 [6]. The results showed that the *Ra* and *MH* were improved by 90.4% and 44.0%, as compared to the initial surface. The optimal parameters were selected to reduce the power consumed and *Ra* of the burnishing AISI 1045 process [7]. The results indicated that the optimal *S*, *f*, and burnishing force were 300 rpm, 0.11 mm/rev, and 130.0 N, respectively. The Taguchi method was used to improve the tribological indicator of the machined EN31 steel [8]. The results showed that the wear resistance was improved by 52.0%, as compared to the turned surface.

A set of experiments was performed to find the modifications of the surface properties of the burnished X2CrNiMo17-12-2 [9]. The authors indicated that the greatest reduction in the *Ra* was obtained. Selma et al. presented that the corrosion resistance of the burnished API 5L X52 was improved by 65.9%, as compared to the initial surface [10]. The sliding roller burnishing method was proposed to improve the surface characteristics of the machined AISI 316 [11]. The authors reported that *Ra* and *MH* were improved by 41.6% and 6.7%, respectively. The optimal parameters were selected to enhance the surface properties of the burnishing metal matrix composite [12]. According to the findings, the optimal *S*, *f*, and allowance were 500 rpm, 0.5 mm/rev, and 0.03 mm, respectively. To improve the burnished 2024-T3 Al alloy's surface quality, the single roller burnishing was suggested [13]. As compared to the traditional one, the improvements in the *MH* and fatigue limit were 37.6% and 35.1%, respectively. The optimal parameters were chosen to improve the tribological indicators of the burnished Ti-6Al-4V [14]. The results showed that 1000 rpm, 0.3 mm, and 5.0 mm were the ideal *S*, *D*, and tool radius, respectively. The *EC* and *Ra* of the burnishing 6061-T6 process were reduced using the ANFIS and PSO [15]. The author presented that the optimal *f* and *D* were 1000 mm/min and 0.07 mm, respectively. The machining responses of the burnishing AISI 4150 operation were improved using optimal parameters [16]. According to the authors, the *EC* and *Ra* were decreased by 16.3% and 24.3%, respectively, while the Rockwell hardness was enhanced by 4.0%.

As a result, different burnishing operations have been considered and optimized. The limitations of the related works can be expressed as below. Firstly, the Taguchi based-optimization approaches have a high risk of falling into local optimal results with experimental data; hence, it is necessary to propose a new optimizing approach. Secondly, the OXGBoost-based predictive models of the *EC*, *Ra*, and *VH* for the roller burnishing AISI 5140 process have not been proposed. Lastly, the ideal burnishing parameters have not been chosen in order to improve outputs.

2. OPTIMIZATION APPROACH

2.1 Process parameters and responses

In this work, the *EC*, *Ra*, and *VH* are addressed and optimized.

The *EC* is computed as:

$$EC = P_t \times t_b \tag{1}$$

where P_t and t_b are the total power consumed and burnishing time, respectively.

The *Ra* is computed as:

$$Ra = \frac{\sum_{i=1}^{3} R_{ai}}{3} \quad (2)$$

where R_{ai} is the main roughness at the i_{th} location.

The *VH* is computed as:

$$VH = \frac{\sum_{i=1}^{3} VH_i}{3} \quad (3)$$

Table 1 displays the process parameters together with their levels. The machine tool's characteristics are used to select the spindle speed and feed rate. The burnishing tool's configuration is used to determine the number of rollers. The manufacturer's recommendation for the burnishing tool is used to choose the depth of penetration.

Table 1. Burnishing process parameters.

Symbol	Parameters	Levels
S	Spindle speed (rpm)	700-950-1200
f	Feed rate (mm/z)	0.05-0.07-0.09
D	Depth of penetration (mm)	0.02-0.04-0.06
N	Number of rollers	3-4-5

2.2 Framework

The optimizing framework of the burnishing process is presented in Fig. 1:

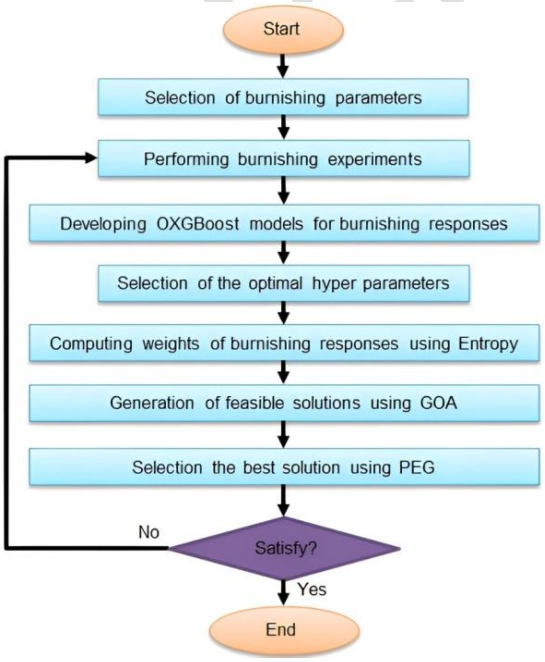

Fig. 1. Optimization approach.

Step 1: The trials are conducted using the Box-Behnken method [17,18]. Four process parameters with three levels requires 25 experiments.

Step 2: The entropy method is used to compute each response's weight.

For a higher approach, the attribute value of each response (r_{ij}) is calculated as:

$$r_{ij} = \frac{x_{ij}}{\max_j x_{ij}}, (i = 1,...,m;\ j = 1,...,n) \quad (4)$$

For a lower the better approach, the r_{ij} is calculated as:

$$r_{ij} = \frac{\min_j x_{ij}}{x_{ij}}, (i = 1,...,m;\ j = 1,...,n) \quad (5)$$

The normalized response (p_{ij}) is calculated as:

$$p_{ij} = \frac{r_{ij}}{\sum_{i=1}^{m} r_{ij}}, (i = 1,...,m;\ j = 1,...,n) \quad (6)$$

The entropy value of the i_{th} objective (E_j) is calculated as:

$$E_j = -\frac{\sum_{j=1}^{m} p_{ij} \times \ln p_{ij}}{\ln m} \quad (7)$$

The entropy weight (ω_i) is calculated as:

$$\omega_i = \frac{1 - E_j}{\sum_{j=1}^{n} (1 - E_j)} \quad (8)$$

Step 3: The XGBoost is used to develop the predictive models of the burnishing responses.

The structure of the XGBoost model having classification and regression trees (CARTs) is presented in Fig. 2, in which each CART contains the root nodes, internal nodes, leaf nodes, and branches. The input is firstly imported into the root node to make the original decision. The internal node is then to make subsequent decision. The leaf nodes represent the prediction results of a single classification and regression tree. The results of all leaf-pointing nodes are combined to obtain the prediction results. The XGBoost model is expressed as:

$$y_i = \alpha \sum_{k=1}^{n} f_k(x_i) \quad (9)$$

where x_i is the input data. α is the learning rate of the individual regression tree, n is the total number of CARTs, f_k is the output of the k_{th} regression tree.

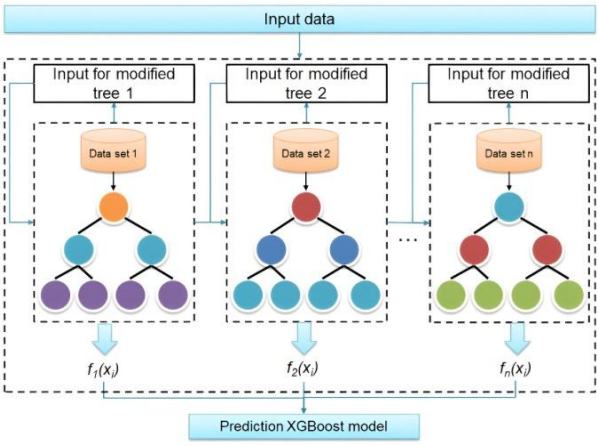

Fig. 2. The scheme of the XGBoost model.

The model's outcome is evaluated using the objective function (L) which is expressed as:

$$L = \sum_{i}^{n} l_k(y_i, y_i) + \sum_{k=1}^{K} \Omega(f_x) \tag{10}$$

where l_k and Ω are the loss function and regularization item, respectively. For each CART, the Ω item is expressed as:

$$\Omega(f) = \gamma T + \frac{1}{2}\lambda \|w\|^2 \tag{11}$$

where T is the number of leaves. γ and λ are penalty coefficients. w is a vector presenting the score of each leaf.

To enhance the accuracy of the predictive outcomes, the hyperparameters of the XGBoost model should be optimized. The hyper parameters considered are the colsample_bytree, learning_rate, max_depth, and subsample. The percentages of the data for the training and testing are 70% and 30%, respectively. The grid search method is employed to find optimal hyper factors. The root Mean square error (RMSE) is used to select the optimal parameters and expressed as:

$$RMSE = \frac{1}{n}\sum_{i=1}^{n}(E_i - P_i)^2 \tag{12}$$

The optimized XGBoost model is evaluated by comparing the predicted results to the actual results from the test dataset. The mean absolute percentage error (MAPE) and the mean absolute error (MAE) are used to evaluate the model's accuracy and expressed as [19,20]:

$$MAE = \frac{1}{n}\sum_{i=1}^{n}\left|EX_i - PD_i\right| \tag{13}$$

$$MAPE = \frac{1}{n}\sum_{i=1}^{n}\left(\frac{\left|EX_i - PD_i\right|}{EX_i}\right)\times 100 \tag{14}$$

where n is number of trials. EX_i and PD_i present experimental and predictive data, respectively.

Step 4: The GOA is used to find the optimal solution. The GOA search process splits into two stages: exploration and exploitation are shown in. In the exploration stage, we update all the positions' values and compute the fitness value of all grasshopper swarms. In the exploitation stage, we find the best solution among all solutions (search for better food sources). In the exploitation stage, the best option in the design space is identified. Every grasshopper represents a solution in the GOA algorithm. The position (X_i) of each solution is expressed as:

$$X_i = S_i + G_i + A_i \tag{15}$$

where S_i is the interaction between the solution and the other swarms. G_i and A_i are the gravity force and the wind advection of the i_{th} solution, respectively (Fig. 3).

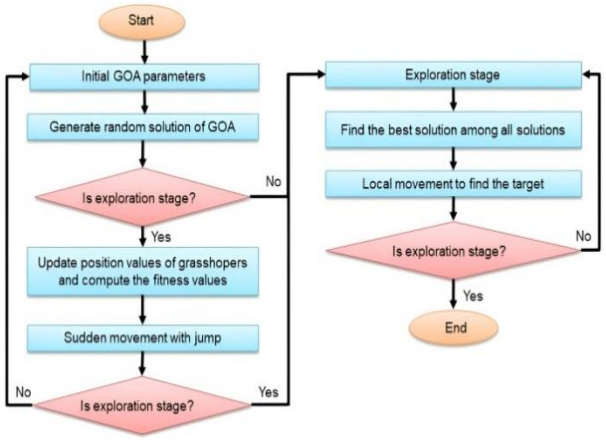

Fig. 3. The working principle of the GOA.

In this work, the distance of grasshoppers' swarms in the range [1,4] is selected to ensure global optimal results.

The S_i is expressed as:

$$S_i = \sum_{j=1}^{N} s(d_{ij}) d_{ij} \quad (16)$$

where N denotes the number of grasshoppers. d_{ij} and d_{ij} are the Euclidean distance between the i_{th} and the j_{th} grasshopper swarm and the unit vector from the i_{th} to the j_{th} grasshopper swarm, respectively.

The G_i is expressed as:

$$G_i = -g e_g \quad (17)$$

where g and e_g present the gravitational constant and unit vector toward center of earth, respectively.

The A_i is expressed as:

$$A_i = u e_w \quad (18)$$

where u and e_w are the drift constant and the unit vector in the wind direction, respectively.

The position (X_i) of each solution is expressed as:

$$X_i = \sum_{j=1}^{N} s(d_{ij}) d_{ij} - g e_g + u e_w \quad (19)$$

The actual equation for solving optimization problems is expressed as:

$$X_i^d = c\left(\sum_{j=1}^{N} c \frac{UB_d - LB_d}{2} s\left(\left|x_j^d - x_i^d\right|\right) \frac{\left|x_j^d - x_i^d\right|}{d_{ij}}\right) + T_d \quad (20)$$

where UB_d and LB_d present the upper and lower data in the dimension space, respectively. T_d denotes the best solution in the dimension space.

Step 5: The best point is determined using PEG. In terms of a higher purpose, the optimal solution is normalized as:

$$X_{i,j} = \min\left(\frac{y_{i,j} - \min(y_i)}{\max(y_i) - \min(y_i)}\right) \quad (21)$$

In terms of a lower purpose, the optimal solution is normalized as:

$$X_{i,j} = \min\left(\frac{\max(y_i) - y_{i,j}}{\max(y_i) - \min(y_i)}\right) \quad (22)$$

The normalized responses are arranged as:

$$x_i = \left[X_i^{\min}, \ldots X_i^{\max}\right]^T = [0, \ldots, 1]^T \quad (23)$$

The aggregate vector is computed as:

$$Y_i = \frac{\sum_{k=1}^{n} x_k - x_i}{n-1} \quad (24)$$

The shifted vectors are computed as:

$$V_x = \frac{x_i + \delta x_i}{1 + \delta x_i}, \; V_y = \frac{y_i + \delta y_i}{1 + \delta y_i} \quad (25)$$

The radial shift is computed as:

$$\Delta r_i = \sqrt{2}\Delta x_i = \sqrt{2}\Delta y_i \quad (26)$$

The decisive function is computed as:

$$f_i^o = f_i^{\max} - (f_i^{\max} - f_i^{\min})(\Delta r_i + \sqrt{2/2}) \quad (27)$$

The decisive score (DS_i) is computed as:

$$DS_i = \frac{1}{\eta} \sum \left(\frac{1 - f_i^*}{f_i^o}\right) \quad (28)$$

Where f_i^* is the experimental response. The best optimality is chosen with the highest DS_i.

3. BURNISHING EXPERIMENTS

The burnishing specimen is the hardened AISI 5140, which is frequently used in automotive and marine parts. The chemical compositions of the AISI 5140 steel are shown in Table 2. The dimensions of each workpiece are as follows: 60.0 mm for length, 13.0 mm for internal diameter, and 28.0 mm for external diameter. The *VH* and *Ra* of the initial specimen are 297.4 HV and 2.62 μm, respectively.

The burnishing experiment is conducted using a CNC milling machine (Fig. 4a). Trials are carried out using a burnishing tool with five movable rollers produced by Cogsdill manufacturer (United States). The burnishing length is 23.0 mm. The rotating motion from the main spindle is transferred via the straight shank.

The power used during the burnishing process is recorded by the power meter (Fig. 4b). The ZeGage Pro 3D and Wolpert testers are used to measure the *Ra* and *VH* data. The testing force and holding time are 300 gf and 10 seconds, respectively (Fig. 4c).

Fig. 5. presents representative experimental data.

Table 2. Chemical compositions of the AISI 5140 steel [21].

Elements	Si	Mn	Cu	Ni	C	P	Cr
%	0.30	0.60	0.30	0.30	0.40	0.035	0.095

(a) Burnishing process (b) Power meter and electrical cabinet (c) The Vickers hardness

Fig. 4. The experimental setting.

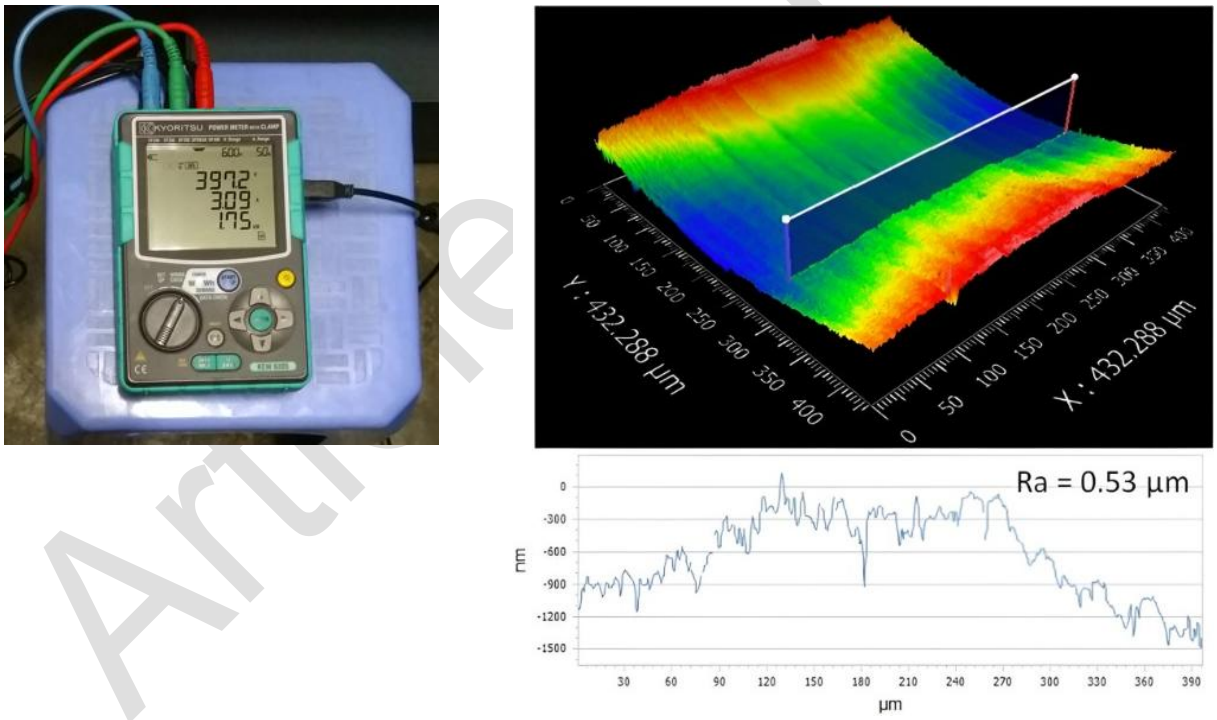

(a) Total power consumed (b) The mean roughness

Fig. 5. The representative data at the No. 6

4. RESULTS AND DISCUSSIONS

4.1 Selection of the best modelling approach

The experimental data of the burnishing process is presented in Table 3.

Table 4 presents the hyperparameters of the XGboost model. The XGBoost models are trained with variations of the hyperparameters. The modifications of the RMS values are shown in Fig. 6. As a result, the optimal *DN*, *LN*, *CB* and *SS* are 3, 0.02, 0.8, and 1.0, respectively.

Table 3. Experimental results of the burnishing operation.

No.	*S* (rpm)	*f* (mm/z)	*D* (mm)	*N*	*EC (kJ)*	*VH* (HV)	*Ra* (μm)
Experimental data for developing models							
1	950	0.05	0.02	4	38.31	374.1	0.54
2	950	0.09	0.02	4	23.74	349.6	0.78
3	950	0.05	0.06	4	42.82	411.7	0.21
4	950	0.09	0.06	4	26.06	383.6	0.52
5	700	0.07	0.04	3	37.27	347.6	0.78
6	700	0.07	0.04	5	42.75	372.6	0.53
7	1200	0.07	0.04	3	25.06	345.2	0.69
8	1200	0.07	0.04	5	27.18	379.7	0.49
9	950	0.07	0.02	3	26.98	337.3	0.76
10	950	0.07	0.02	5	31.62	387.8	0.53
11	950	0.07	0.06	3	31.23	393.7	0.45
12	950	0.07	0.06	5	34.19	402.9	0.26
13	700	0.05	0.04	4	51.22	370.7	0.57
14	1200	0.05	0.04	4	34.02	377.5	0.47
15	700	0.09	0.04	4	32.26	348.5	0.82
16	1200	0.09	0.04	4	21.67	346.6	0.75
17	700	0.07	0.02	4	37.72	338.4	0.83
18	1200	0.07	0.02	4	23.52	339.8	0.73
19	700	0.07	0.06	4	40.83	373.3	0.53
20	1200	0.07	0.06	4	27.25	376.4	0.45
21	950	0.05	0.04	3	39.02	382.1	0.48
22	950	0.05	0.04	5	43.60	412.6	0.27
23	950	0.09	0.04	3	24.14	356.4	0.75
24	950	0.09	0.04	5	27.14	385.6	0.55
25	950	0.07	0.04	4	30.53	369.2	0.43
Experimental data for testing the accuracy of the developed models							
26	750	0.06	0.03	3	39.14	347.1	0.75
27	800	0.08	0.05	4	32.21	368.1	0.54
28	900	0.07	0.03	5	34.01	387.8	0.46
29	1000	0.07	0.05	3	29.14	376.2	0.49
30	1050	0.08	0.04	4	25.06	361.9	0.52
31	1150	0.06	0.05	5	32.89	399.1	0.31
32	900	0.06	0.06	3	37.24	401.6	0.41
33	800	0.05	0.03	4	45.43	373.6	0.53
34	1000	0.08	0.04	5	28.19	386.8	0.45
35	1150	0.06	0.05	3	30.45	375.5	0.51

Table 4. Hyperparameters of the XGboost model.

No.	Symbols	Hyperparameters	Ranges	Default	Tolerance
1	*DM*	max_depth	3-10	6	1
2	*LN*	learning_rate	0.1-0 .5	0.3	0.05
3	*CB*	colsample_bytree	0.4-1	1	0.1
4	*SS*	subsample	0.2-1	1	0.1

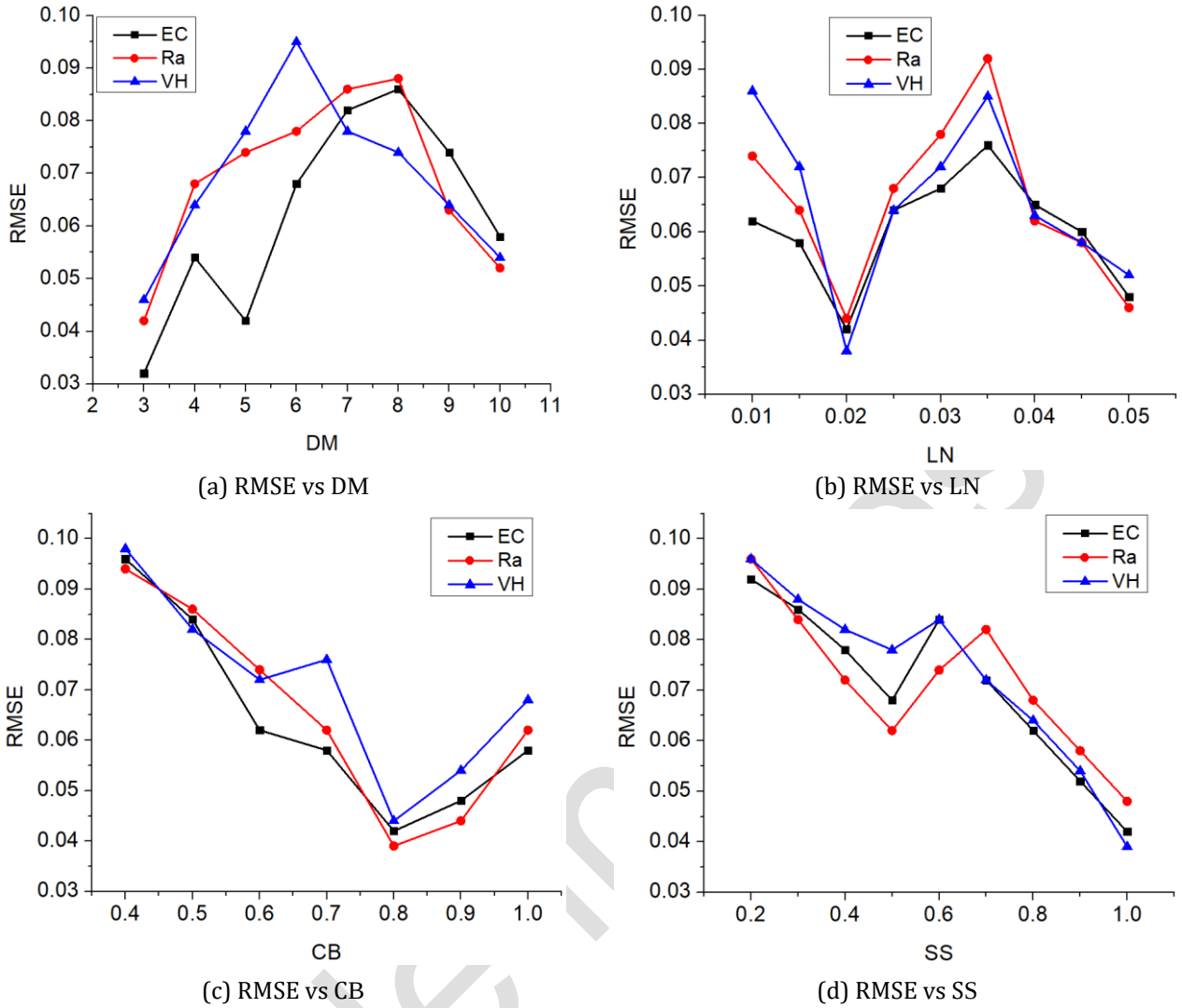

(a) RMSE vs DM

(b) RMSE vs LN

(c) RMSE vs CB

(d) RMSE vs SS

Fig. 6. RMSE and XGBoost hyperparameters.

The MAPE, MAE, and RMSE values of the unoptimal and OXGboost models are presented in Table 5. The MAPE, MAE, and RMSE values of the OXGboost model are lower than the unoptimized ones. The R^2 values of the OXGboost models are higher than unoptimized correlations.

Table 5. Performance evaluations of different models.

Responses	Models	Statistical metrics			
		MAE	MAP	RMSE	R^2
EC	Optimized XGB model	0.0284	0.0664	0.0522	0.9752
	Unoptimized XGB model	0.0886	0.0962	0.0774	0.9503
Ra	Optimized XGB model	0.0302	0.0681	0.0426	0.9748
	Unoptimized XGB model	0.0863	0.0962	0.0726	0.9486
VH	Optimized XGB model	0.0232	0.0523	0.0412	0.9728
	Unoptimized XGB model	0.0946	0.1024	0.0536	0.9438

Table 6 presents the comparisons between the experiments and XGBoost-predicted outcomes. As a result, the errors of the *EC*, *Ra*, and *VH* models lie from -0.78 to 0.75%, -0.58 to 0.23%, and -3.23 to 2.17%, respectively. The small errors indicate that the accuracy of the developed models is acceptable. Fig. 7 presents the comparisons between the predictive and actual values for the burnishing responses. The adequate XGBoost models are observed with consistent data.

Table 6. Testing the accuracy of the developed XGBoost models.

No.	*EC* (kJ)			*VH* (HV)			*Ra* (μm)		
	Actual	Pre.	Err. (%)	Actual	Pre.	Err. (%)	Actual	Pre.	Err. (%)
26	39.14	39.23	-0.23	347.1	348.1	-0.29	0.75	0.74	1.33
27	32.21	32.46	-0.78	368.1	370.1	-0.54	0.54	0.55	-1.85
28	34.01	34.16	-0.44	387.8	388.2	-0.10	0.46	0.45	2.17
29	29.14	28.92	0.75	376.2	378.4	-0.58	0.49	0.48	2.04
30	25.06	25.24	-0.72	361.9	363.8	-0.53	0.52	0.51	1.92
31	32.89	32.76	0.40	399.1	398.2	0.23	0.31	0.32	-3.23
32	37.24	37.06	0.48	401.6	402.8	-0.30	0.41	0.42	-2.44
33	45.43	45.76	-0.73	373.6	375.1	-0.40	0.53	0.52	1.89
34	28.19	28.31	-0.43	386.8	388.6	-0.47	0.45	0.46	-2.22
35	30.45	30.64	-0.62	375.5	377.1	-0.43	0.51	0.52	-1.96

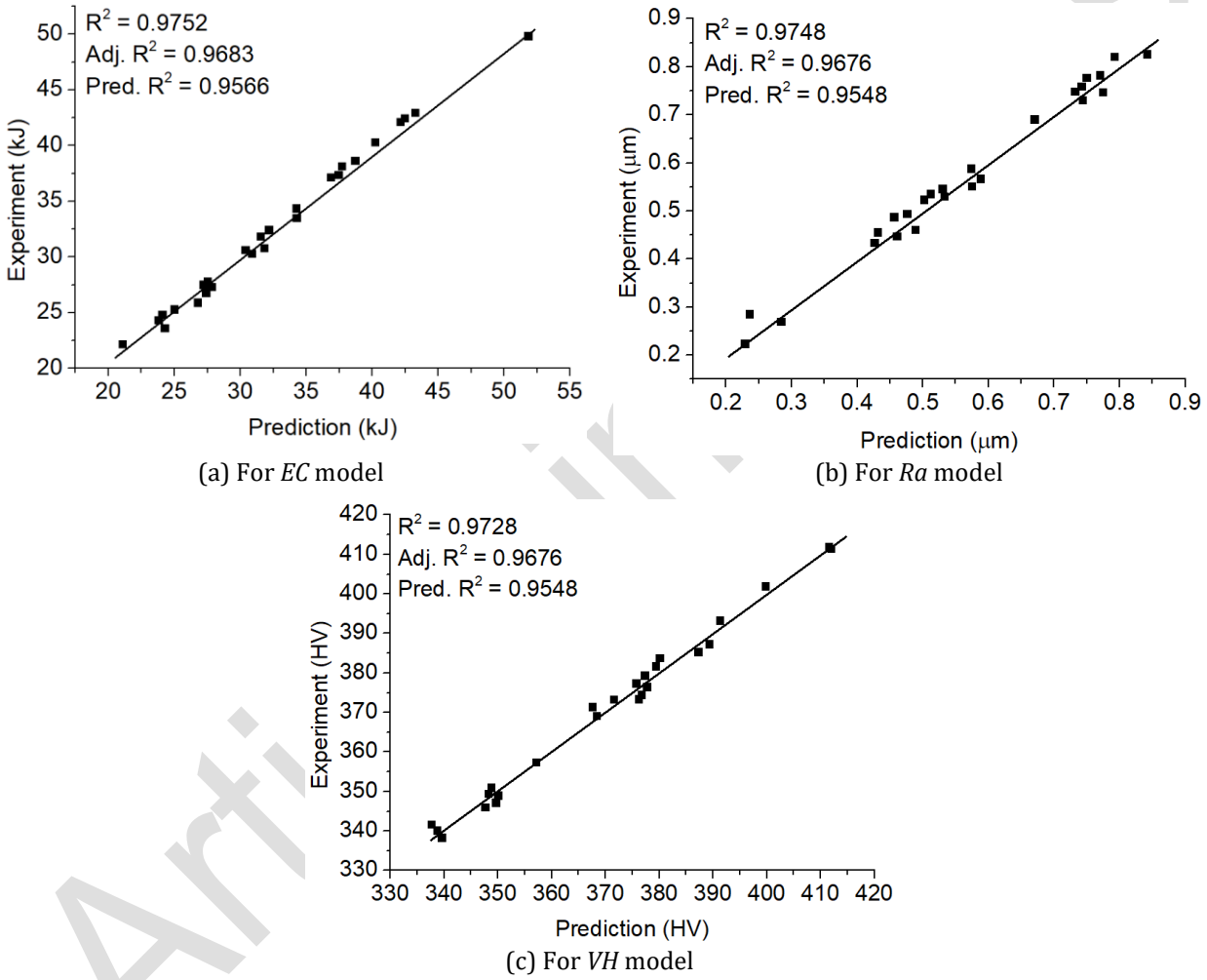

(a) For *EC* model (b) For *Ra* model

(c) For *VH* model

Fig. 7. Comparisons between the predictive and actual values for burnishing responses.

4.2 ANOVA analysis for burnishing responses

ANOVA results for the *EC* are shown in Table 7. As a result, the significant factors having p-values less than 0.05 are the *S*, *f*, *D*, *N*, *Sf*, *SN*, *fD*, *FN*, *DN*, S^2, f^2, and N^2. The contributions of the *S*, *f*, *D*, and *N* are 25.34%, 28.56%, 6.23%, and 6.92%, respectively. The contributions of the *Sf*, *SN*, *fD*, *fN*, and *DN* are 6.03%, 3.07%, 2.06%, 1.43%, and 1.53%, respectively. The contributions of the S^2, f^2, and N^2 are 7.05%, 8.52%, and 2.21%, respectively.

ANOVA results for the *Ra* are shown in Table 8. As a result, the significant factors having p-values less than 0.05 are the *S*, *f*, *D*, *N*, *Sf*, *fD*, *DN*, S^2, f^2, D^2, and N^2. The contributions of the *S*, *f*, *D*, and *N* are 6.01%, 17.94%, 19.14%, and 13.34%, respectively. The contributions of the *fQ*, *fD*, and *DN* are 1.31%, 1.96%, and 1.39%, respectively.

The contributions of the S^2, f^2, D^2, and N^2 are 22.53%, 6.29%, 4.48%, and 4.64%, respectively.

Table 7. ANOVA results for the EC model.

So.	SS	MS	F Value	P-value	Remark
Mo.	1430.01	102.14	65.90	< 0.0001	Sig.
S	3675.71	3675.71	2371.43	< 0.0001	Sig.
f	4142.79	4142.79	2672.77	< 0.0001	Sig.
D	903.70	903.70	583.03	< 0.0001	Sig.
N	1003.79	1003.79	647.60	< 0.0001	Sig.
Sf	874.69	874.69	564.31	< 0.0001	Sig.
SD	81.23	81.23	52.41	0.4515	Insig.
SN	445.32	445.32	287.30	0.0008	Sig.
fD	298.81	298.81	192.78	0.0013	Sig.
fN	211.78	211.78	136.63	0.0022	Sig.
DN	221.94	221.94	143.18	0.0021	Sig.
S^2	1022.64	1022.64	659.77	< 0.0001	Sig.
f^2	1235.87	1235.87	797.34	< 0.0001	Sig.
D^2	66.73	66.73	43.05	0.4252	Insig.
N^2	320.57	320.57	206.82	0.0011	Sig.
Re.	21.70	1.55			
Cor.	1466.37				
R^2 = 0.9752; Adj. R^2 = 0.9683; Pred. R^2 = 0.9566					

Table 8. ANOVA results for the Ra model.

So.	SS	MS	F Value	P-value	Remark
Mo.	0.81015	0.0579	38.58	< 0.0001	Sig.
S	0.12218	0.1222	81.45	< 0.0001	Sig.
f	0.36470	0.3647	243.14	< 0.0001	Sig.
D	0.38910	0.3891	259.40	< 0.0001	Sig.
N	0.27119	0.2712	180.79	< 0.0001	Sig.
Sf	0.02663	0.0266	17.75	0.0015	Sig.
SD	0.00651	0.0065	4.34	0.8366	Insig.
SN	0.00000	0.0000	0.00	1.0000	Insig.
fD	0.03984	0.0398	26.56	0.0012	Sig.
fN	0.01321	0.0132	8.81	0.6806	Insig.
DN	0.02826	0.0283	18.84	0.0016	Sig.
S^2	0.45801	0.4580	305.34	< 0.0001	Sig.
f^2	0.12787	0.1279	85.25	< 0.0001	Sig.
D^2	0.09107	0.0911	60.72	< 0.0001	Sig.
N^2	0.09433	0.0943	62.88	< 0.0001	Sig.
Re.	0.02094	0.0015			
Cor.	0.83110				
R^2 = 0.9748; Adj. R^2 = 0.9676; Pred. R^2 = 0.9548					

ANOVA results for the *VH* are shown in Table 9. As a result, the significant factors having p-values less than 0.05 are the *S*, *f*, *D*, *N*, *Sf*, *SN*, *DN*, S^2, f^2, D^2, and N^2. The contributions of the *S*, *f*, *D*, and *N* are 1.14%, 13.49%, 18.33%, and 15.32%, respectively. The contributions of the *Sf*, *SN*, and *DN* are 2.17%, 2.36%, and 10.56%, respectively. The contributions of the S^2, f^2, D^2, and N^2 are 16.06%, 7.32%, 3.50%, and 8.02%, respectively.

Table 9. ANOVA results for the VH model.

So.	SS	MS	F Value	P-value	Remark
Mo.	11773.64	840.97	35.77	< 0.0001	Sig.
S	309.59	309.59	13.17	0.0008	Sig.
f	3663.43	3663.43	155.82	< 0.0001	Sig.
D	4977.81	4977.81	211.73	< 0.0001	Sig.
N	4160.40	4160.40	176.96	< 0.0001	Sig.
Sf	589.30	589.30	25.07	0.0028	Sig.
SD	124.92	124.92	5.31	0.7873	Insig.
SN	640.90	640.90	27.26	0.0026	Sig.
fD	249.84	249.84	10.63	0.0595	Insig
fN	95.05	95.05	4.04	0.8236	Insig.
DN	2867.74	2867.74	121.98	< 0.0002	Sig.
S^2	4361.36	4361.36	185.51	< 0.0001	Sig.
f^2	1987.87	1987.87	84.55	< 0.0002	Sig.
D^2	950.48	950.48	40.43	< 0.0003	Sig.
N^2	2177.96	2177.96	92.64	< 0.0004	Sig.
Re.	329.20	23.51			
Cor.	12102.83				
R^2 = 0.9728; Adj. R^2 = 0.9646; Pred. R^2 = 0.9504					

4.3 Impacts of process parameters on the burnishing responses

Fig. 8 shows the main impacts of burnishing factors on the *EC*. When the *S* increases from 700 to 1200 rpm, the *EC* decreases by 21.9% (Fig. 8a). A greater *S* raises the burnishing frequency, which increases the machining region's temperature. The *EC* reduces as a result of the specimen's decreased strength and hardness. When the *f* increases from 0.05 to 0.09 mm/z, the *EC* decreases by 23.2% (Fig. 8a). A greater *f* shortens the burnishing tine and a lower *EC* is used. In practice, a greater *f* results in low resistance between the specimen and the burnishing tool; as a result, the *EC* decreases. When the *D* increases from 0.02 to 0.06 mm, the *EC* increases by 17.1% (Fig. 8b). Greater resistance results from a higher *D*, leading to higher energy to overcome the friction. A 9.7% increase in *EC* occurs when the *N* changes from 3 to 5 (Fig. 8b). To overcome the friction, a higher *EC* is needed due to greater resistance produced by an increase in the *N*.

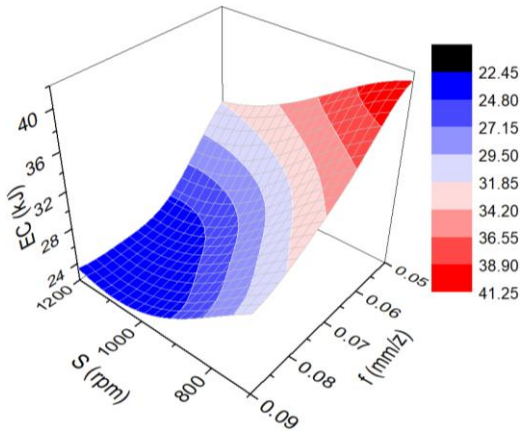

(a) *EC* versus *S* and *f*

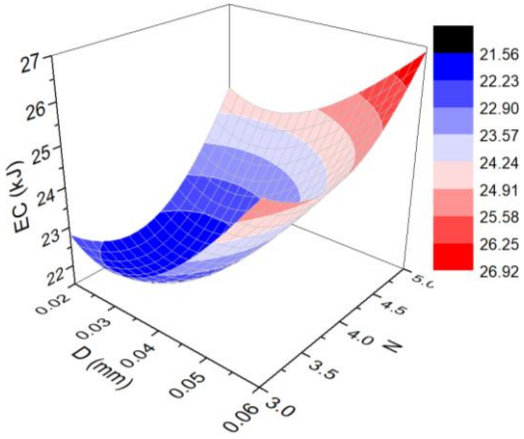

(b) *EC* versus *D* and *N*

Fig. 8. The interactive impacts of process parameters on the *EC.*

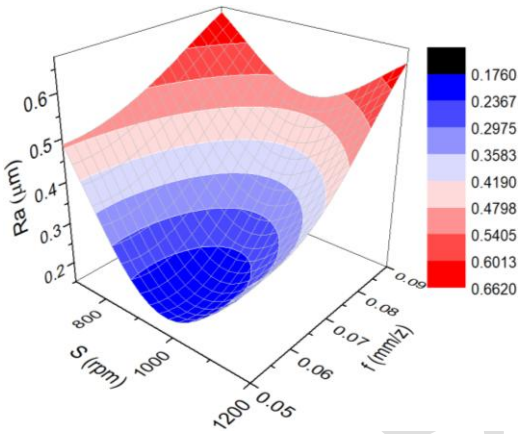

(a) *Ra* versus *S* and *f*

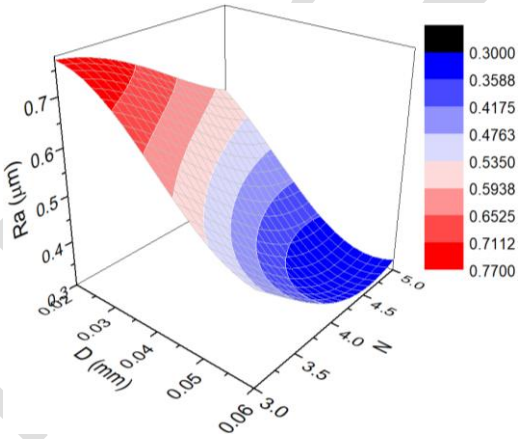

(b) *Ra* versus *D* and *N*

Fig. 9. The interactive impacts of process parameters on the *Ra.*

The effects of the process parameters on the *Ra* are shown in Fig. 9. When the *S* increases from 700 to 970 rpm, the *Ra* decreases by 12.7% (Fig. 9a). On the other hand, when the *S* increases from 9700 to 1200 rpm, the *Ra* increases by 8.1%. As the *S* increases, the machining temperature grows, the workpiece's strength and hardness diminish. The material is easily burnished and the *Ra* is significantly reduced. A further S causes work-hardening behavior; hence, a low *Ra* is produced. When the *f* increases from 0.05 to 0.09 mm/z, the *Ra* increases by 27.3% (Fig. 9a). *Ra* rises when *f* increases because there is more material left over after two consecutive machining operations. When the *D* increases from 0.02 to 0.06 mm, the *Ra* decreases by 23.9% (Fig. 9b). Deeper burnishing results in a greater degree of plastic deformation and higher machining pressure. *Ra* decreases when more material is burnished. When the *N* increases from 3 to 5, the *Ra* decreases by 26.9% (Fig. 9b). *Ra* decreases as a result of increased material compression produced by an increase in the *N*.

Fig. 10 presents the impact of the process parameters on the *VH*. When the *S* increases from 700 to 950 rpm, the *VH* increases by 2.4% (Fig. 10a). In comparison, when the *S* increases from 9500 to 1200 rpm, the *VH* decreases by 2.6%. Increased machining engagement from a higher *S* raises the temperature. Higher *VH* is obtained as a result of the increased degree of plastic deformation that makes material compression easier. However, a further *S* results in higher machining temperatures, which relieve residual stress; hence, a lower *VH* is produced. When the *f* increases from 0.05 to 0.09 mm/z, the *VH* decreases by 3.3% (Fig. 10a). A higher *f* reduces the degree of material compression, leading to a lower *VH*. When the *D* increases from 0.02 to 0.06 mm, the *VH* increases by 8.1% (Fig. 10b). A higher *D* increases the burnishing pressure on the workpiece's surface, leading to a higher degree of plastic deformation; hence, the *VH* increases. When the *N* increases from 3 to 5, the *VH* increases by 6.4% (Fig. 10b). A higher *VH* is created because an increase in *N* causes a higher degree of material compression.

Table 10. Optimization results produced by the GOA.

Method	Optimization parameters				Responses			DS_i
	S (rpm)	*f* (mm/z)	*D* (mm)	*N*	*EC (kJ)*	*VH* (HV)	*Ra* (µm)	
Initial values	950	0.07	0.04	4	30.53	369.2	0.43	
GOA	1075	0.07	0.06	4	28.87	387.9	0.33	0.732
Improvement (%)					5.4	5.1	23.3	

Table 11. Comparisons between pre-machined and machined surface.

Surface characteristics	*VH (HV)*	*Ra (µm)*
Pre-burnished	297.4	2.62
Burnished surface	387.9	0.33
Improvements (%)	30.4	-87.4

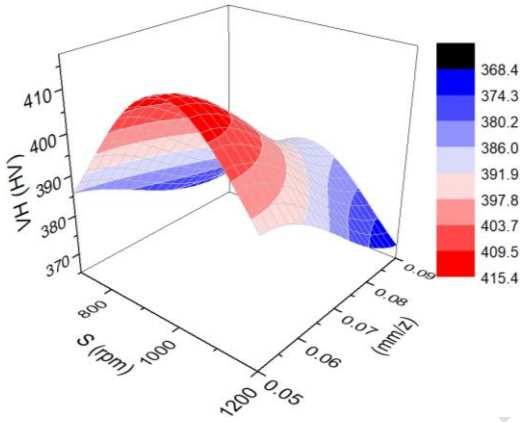

(a) *VH* versus *S* and *f*

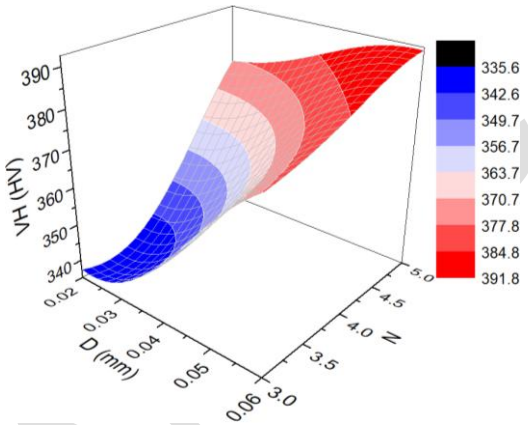

(b) *VH* versus *D* and *N*

Fig. 10. The interactive impacts of process parameters on the *VH.*

4.4 Optimal outcomes produced by the GOA

The computed weights of the *EC*, *Ra*, and *VH* are 0.34, 0.35, and 0.32, respectively. Fig. 11 shows the Pareto graphs produced by GOA. The highest DS_i is utilized to find the best optimal solution. The best results produced by the *S*, *f*, *D*, and *N* are 1075 rpm, 0.07 mm/z, 0.06 mm, and 4, respectively (Table 10). At the selected solution, the *VH* is improved by 5.1%, while the *EC* and *Ra* are reduced by 5.4% and 23.3%, respectively. The *VH* is enhanced by 30.4% and the *Ra* is reduced by 87.4%, respectively, as compared to the milled surface (Table 11).

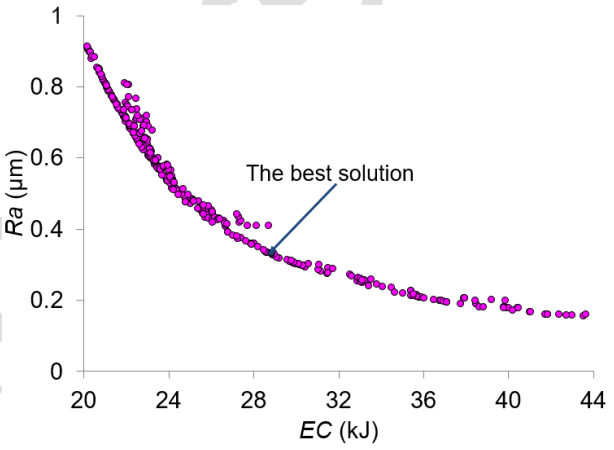

(a) *EC* versus *Ra*

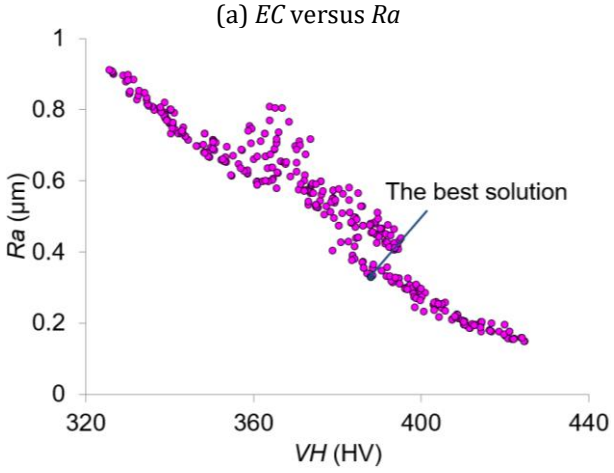

(b) *VH* versus *Ra*

Fig. 11. Pareto fronts produced by the GOA.

4.5 Scientific and industrial contributions

Firstly, the developed optimization approach, comprising OXGBoost, the entropy method, the GOA, and PEG, is effectively used to solve complex problems in other burnishing processes.

Secondly, the optimal process parameters and burnishing responses can be selected for different machining objectives using the Pareto graphs generated by the GOA.

Thirdly, the OXGBoost approach was effectively used to present the highly nonlinear data, and the GOA was efficiently utilized to find global optimal results.

Finally, the developed roller burnishing process is effectively used to produce high-quality internal surfaces.

5. CONCLUSIONS

In this work, the process parameters, including the *S*, *f*, *D*, and *N* were optimized to reduce the *EC* as well as *Ra* and improve the *VH* of the burnishing AISI 5140 process. The prediction models of the performances were proposed using the XGBoost approach. The weight of each response was determined using the Entropy method. The optimum optimality was determined using the GOA and PEG. The results are expressed as:

1. Higher values of the *S* and *f* could be used to reduce the *EC*, while lower values of the *D* and *N* were recommended. Higher values of the *S*, *D*, and *N* could be used to reduce the *Ra*, while a low *f* was recommended. Higher values of the *S*, *D*, and *N* could be used to enhance the *VH*, while a low *f* was recommended.
2. The *EC* model was primarily affected by the *f*, followed by the *S*, *N*, and *D*, respectively. The Ra model was primarily affected by the *D*, *f*, *N*, and *S*, respectively. The Vickers hardness model was primarily affected by the *D*, *N*, *f*, and *S*, respectively.
3. The optimal *S*, *f*, *D*, and *N* were 1075 rpm, 0.07 mm/z, 0.06 mm, and 4, respectively. At the selected solution, the *VH* was enhanced by 5.1%, while the *EC* and *Ra* were decreased by 5.4% and 23.3%, respectively.
4. The optimal data are effectively used to enhance the surface properties and decrease energy consumed the practical burnishing AISI 5140 process.

Abbreviations

OXGBoost		Extreme Gradient Boosting
GOA		Grasshopper Optimization Algorithm
S	rpm	Spindle speed
f	mm/z	Feed rate
D	mm	Depth of penetration
VH	HV	Vickers hardness
EC	kJ	Energy consumption
Ra	μm	Average surface roughness
PEG		Pareto-Edgeworth Grierson
N		Number of rollers
MH	HV	Micro hardness
RSM		Response surface method

REFERENCES

[1] K. A. Prasad and M. R. S. John, "Optimization of external roller burnishing process on magnesium silicon carbide metal matrix composite using response surface methodology," *Journal of the Brazilian Society of Mechanical Sciences and Engineering*, vol. 43, p. 342, Jun. 2021, doi: 10.1007/s40430-021-03069-3.

[2] I. Beşliu-Băncescu and L. Slătineanu, "Influence of machining environments on the burnishing performance of aluminum alloy EN AW-2007," *Lubricants*, vol. 13, no. 8, p. 368, Jul. 2025, doi: 10.3390/lubricants13080368.

[3] M. Boozarpoor and R. Teimouri, "Parametric study of multi-roller rotary burnishing process," *International Journal of Lightweight Materials and Manufacture*, vol. 4, no. 2, pp. 179–194, Jun. 2021, doi: 10.1016/j.ijlmm.2020.10.001.

[4] J. Zhi-Guo et al., "Enhanced Wear Resistance of 20Cr2Ni4A Steel under Starved Lubrication Conditions via Ultrasonic Surface Burnishing Process," *Journal of Materials Engineering and Performance*, vol. 34, no. 14, pp. 14005–14016, Dec. 2024, doi: 10.1007/s11665-024-10209-y.

[5] A. M. Mebarek, M. Bourebia, L. Laouar, *et al.*, "Effect of ball burnishing process on surface roughness and corrosion behavior of S235JR steel," *International Journal of Advanced Manufacturing Technology*, vol. 130, pp. 3431–3444, Jan. 2024, doi: 10.1007/s00170-023-12906-9.

[6] H. Roohi, J. Baseri, and M. J. Mirnia, "Experimental study of slide burnishing process of the pre-milled AA7075 plate: Surface topography and hardening aspects," *Arabian Journal for Science and Engineering*, Nov. 2024, doi: 10.1007/s13369-024-09784-y.

[7] K. Bousnina, W. Tarhouni, A. Hamza, *et al.*, "Experimental modeling and optimization of surface quality and energy consumption in the roller burnishing process of AISI 1045 steel using intelligent models," *International Journal of Advanced Manufacturing Technology*, vol. 139, pp. 3419–3433, Jul. 2025, doi: 10.1007/s00170-025-16126-1.

[8] N. J. Varpe and A. Hamilton, "Investigation into burnishing process to examine effect on surface integrity, wear and corrosion resistance of carbon alloy (EN31) steel," *Journal of Materials Engineering and Performance,* vol. 33, pp. 3691–3705, Oct. 2024, doi: 10.1007/s11665-023-08524-x.

[9] T. Dyl, D. Rydz, A. Szarek, *et al.*, "The influence of slide burnishing on the technological quality of X2CrNiMo17-12-2 steel," *Materials*, vol. 17, p. 3403, Jul. 2024, doi: 10.3390/ma17143403.

[10] B. Selma, H. Hamid, T. Ouahiba, *et al.*, "Impact of burnishing techniques on corrosion resistance in pipeline materials," *International Journal of Advanced Manufacturing Technology*, vol. 138, pp. 1591–1604, May 2025, doi: 10.1007/s00170-025-15605-9.

[11] J. Maximov, G. Duncheva, A. Anchev, *et al.*, "Effect of roller burnishing and slide roller burnishing on surface integrity of AISI 316 steel: Theoretical and experimental comparative analysis," *Machines*, vol. 12, p. 51, Jan. 2024, doi: 10.3390/machines12010051.

[12] K. R. Arun Prasad and M. R. Stalin John, "An optimisation of the internal roller burnishing process for magnesium composites using Taguchi multi-objective optimization method," *Materials Science and Technology*, vol. 40, no. 17, pp. 1297–1305, Oct. 2024, doi: 10.1177/02670836241273485.

[13] G. V. Duncheva, J. T. Maximov, V. P. Dunchev, *et al.*, "Single toroidal roller burnishing of 2024-T3 Al alloy implemented as mixed burnishing process," *International Journal of Advanced Manufacturing Technology*, vol. 111, pp. 3559–3570, Nov. 2020, doi: 10.1007/s00170-020-06350-2.

[14] G. Rotella, S. Caruso, A. Del Prete, *et al.*, "Prediction of surface integrity parameters in roller burnishing of Ti6Al4V," *Metals*, vol. 10, p. 1671, Dec. 2020, doi: 10.3390/met10121671.

[15] R. Teimouri and S. Amini, "A comprehensive optimization of ultrasonic burnishing process regarding energy efficiency and workpiece quality," *Surface and Coatings Technology*, vol. 375, pp. 229–242, Oct. 2019, doi: 10.1016/j.surfcoat.2019.07.038.

[16] T. T. Nguyen and M. T. Le, "Optimization of the internal roller burnishing process for energy reduction and surface properties," *Strojniški vestnik – Journal of Mechanical Engineering*, vol. 67, no. 4, pp. 167–179, Apr. 2021, doi: 10.5545/sv-jme.2021.7106.

[17] P. Laura, V. M. Rodríguez, D. Maldonado-Cortés, *et al.*, "Optimizing milling parameters and halloysite nanotube concentration to enhance surface quality and reduce energy consumption," *Tribology in Industry*, vol. 47, no. 2, pp. 313–325, Apr. 2025, doi: 10.24874/ti.1896.02.25.04.

[18] N. W. Ken, W. Job, and M. M. Fredrick, *et al.*, "Evaluation of surface quality and productivity in conventional milling of copper beryllium using minimum quantity lubrication," *Tribology in Industry*, vol. 46, no. 3, pp. 355–367, Jun. 2024, doi: 10.24874/ti.1566.10.23.01.

[19] D. Sahu, R. D. Kumar, and S. P. Singh Matharu, "Comparative analysis of machine learning techniques for fault diagnosis of rolling element bearing with wear defects," *Tribology in Industry*, vol. 47, no. 1, pp. 151–163, Mar. 2025, doi: 10.24874/ti.1749.09.24.12.

[20] S. Slawomir, "Engine health status prediction based on oil analysis with augmented machine learning algorithms," *Tribology in Industry*, vol. 46, no. 4, pp. 624–638, Dec. 2024, doi: 10.24874/ti.1736.08.24.09.

[21] L. Tian, G. Su, Y. Xia, *et al.*, "Improving the dry machining performance of AlCrN-coated tool through femtosecond laser textures combined with DLC self-lubricating coatings," *Journal of Materials Engineering and Performance*, Sep. 2025, doi: 10.1007/s11665-025-12001-y.